

PAPER

Inter-ELM pedestal evolution on MAST and impact of resonant magnetic perturbations

To cite this article: R Scannell *et al* 2013 *Plasma Phys. Control. Fusion* **55** 035013

View the [article online](#) for updates and enhancements.

Related content

- [Understanding edge-localized mode mitigation by resonant magnetic perturbations on MAST](#)
A. Kirk, I.T. Chapman, Yueqiang Liu *et al.*
- [Effect of resonant magnetic perturbations on ELMs in connected double null plasmas in MAST](#)
A Kirk, Yueqiang Liu, I T Chapman *et al.*
- [Effect of resonant magnetic perturbations with toroidal mode numbers of 4 and 6 on edge-localized modes in single null H-mode plasmas in MAST](#)
A Kirk, I T Chapman, J Harrison *et al.*

Recent citations

- [Preliminary Study of the Magnetic Perturbation Effects on the Edge Density Profiles and Fluctuations Using Reflectometers on EAST](#)
Gao Yu *et al*
- [Modelling of edge localised modes and edge localised mode control](#)
G. T. A. Huijsmans *et al*
- [Overview of MAST results](#)
I.T. Chapman *et al*



IOP | ebooks™

Bringing you innovative digital publishing with leading voices to create your essential collection of books in STEM research.

Start exploring the collection - download the first chapter of every title for free.

Inter-ELM pedestal evolution on MAST and impact of resonant magnetic perturbations

R Scannell, A Kirk and I T Chapman

EURATOM/CCFE Fusion Association, Culham Science Centre, Abingdon, Oxon OX14 3DB, UK

E-mail: roby.scannell@ccfe.ac.uk

Received 12 November 2012, in final form 18 January 2013

Published 15 February 2013

Online at stacks.iop.org/PPCF/55/035013

Abstract

The peak pressure gradient in the pedestal ($dP_e/d\psi$) on MAST varies little between edge localized modes (ELMs), although it varies between discharges due to factors such as gas fuelling and plasma current. The pressure pedestal width in flux space on the high-field side (HFS), both during the inter-ELM period and amongst different plasma discharges is consistent with a scaling of $\Delta_{pe} \approx 0.07\beta_\theta^{1/2}$. In flux space very similar $dP_e/d\psi$ and Δ_{pe} are observed on the HFS and low-field side (LFS) in single null configuration. This symmetry is broken by the application of resonant magnetic perturbations (RMPs). During ELM mitigation by application of RMPs changes in the edge transport barrier position and width are observed. These changes are dependent on the intensity of the RMP and on the toroidal location with respect to the RMP phase. An outward displacement of up to 30 mm and increase in the edge pedestal width of up to 50% with respect to the coils case off are observed. Increased particle transport causes a decrease in $n_{e,ped}$, and hence $P_{e,ped}$, as is observed on other devices. The combination of an increase in Δ_{pe} on the LFS and decrease in $P_{e,ped}$ results in significantly reduced LFS $dP_e/d\psi$ when these perturbations are applied to the plasma edge. A decrease in $dP_e/d\psi$ on the HFS is also observed due to RMP; however, this decrease is caused solely by the $P_{e,ped}$ decrease whilst no expansion of Δ_{pe} on the HFS is observed.

(Some figures may appear in colour only in the online journal)

1. Introduction

Significant research effort has focused on using the pedestal height and width observed on current devices to predict pedestal and hence core plasma performance on future devices [1–4]. Improved pedestal performance implies increased $P_{e,ped}$, which in turn can increase particle and heat flux during edge localized modes (ELMs). Recent experiments have used resonant magnetic perturbations (RMPs) applied to the plasma edge to mitigate and suppress ELMs [5–7] and increasingly there is a focus on the impact of RMPs on the pedestal [8, 9]. The aim of the work presented here is to examine the implication of RMPs on the MAST pedestal behaviour, particularly looking at the impact on pedestal width and sustainable pressure gradients in the edge transport barrier. This paper initially focuses on observations of the pedestal in a number of ELMing plasmas with no

RMP and subsequently observations in plasmas with various configurations and intensities of RMP.

A typical MAST type-I ELMing discharge is analysed in some detail [10]. Stability analysis of this case has shown that this plasma becomes unstable to finite- n ballooning modes at the end of the inter-ELM period, triggering the ELM. However, it is the decreasing stability limit due to the region of high pressure gradient moving inwards, rather than increasing magnitude of the pressure gradient that triggers the ELM. The high gradient region is unstable to $n = \infty$ ballooning modes throughout the inter-ELM period. Gyrokinetic analysis [10] has shown that this region which is unstable to $n = \infty$ ballooning modes corresponds well to the region unstable to kinetic ballooning modes (KBMs), making these modes the likely candidate for limiting the pressure gradient within the edge transport barrier. In the first part of this paper, we compare the inter-ELM pedestal evolution of the standard

MAST discharge with discharges with varying collisionality and magnetic configuration.

A number of tokamaks have demonstrated ELM mitigation due to RMP in the form of a large increase in ELM frequency [6, 11]. This increased ELM frequency causes a decrease in energy per ELM and hence decreased power loads on plasma-facing components. ELM suppression due to RMP, complete removal of type-I ELMs, has been achieved in DIII-D [5] and mitigation to very small ELMs on ASDEX Upgrade [7]. Although suppression is typically the ultimate goal, it may be on future devices that a regime including ELM mitigation is used either due to the inability to completely suppress ELMs or because some ELMs are required for impurity control. On MAST application of RMPs causes ELM mitigation, though complete suppression has not yet been observed [6]. The impact of $n = 6$ RMP on the pedestal of a single null plasma is the focus of section 3 of this paper, detailing the impact on the radial profiles, evolution of pedestal parameters between ELMs and high-field side (HFS) low-field side (LFS) symmetry. For comparison purposes all of the RMP pulses are paired with equivalent pulses which have no applied RMP, but are otherwise identical. The final part of the paper examines the impact of two phases of applied RMP on a double null (DND) plasma, where phase is the toroidal modulation of the RMP with respect to the fixed toroidal location of Thomson scattering (TS) measurement.

The data presented here are predominantly taken from the MAST TS system [12], which measures with better than 10 mm resolution across the full plasma radius. In all cases the data are deconvolved following the procedure outlined in [13] to remove the impact of the instrument function. Deconvolution does not impact on the conclusions from the results discussed in this paper. In this deconvolution procedure, the fits are performed to $T_e(r)$ and $n_e(r)$ in real space, where the instrument function can be removed, the results are then mapped to flux space where the pressure profile is then fitted. Hence throughout this paper the density and temperature pedestal widths (Δ_{T_e} and Δ_{n_e}) are referred to in real space and the pressure pedestal width ($\Delta_{pe,\psi}$) is referred to in flux space. The same trends of pedestal width expansion with β_{poloidal} and width expansion due to application of ELM coils are observed in the profiles in both real and flux space. Fitting to the edge radial profiles is performed using the modified \tanh function [14] and the pedestal width, height and position obtained from these fits are used throughout this paper.

2. Edge evolution in the inter-ELM period

In the period between typical MAST type-I ELMs [10] an increase in $P_{e,\text{ped}}$, an increase in $\Delta_{pe,\psi}$ and inward movement of the transport barrier position are observed. The combination of increasing $P_{e,\text{ped}}$ and expanding $\Delta_{pe,\psi}$ results in only a small change in peak pressure gradient between ELMs. The inter-ELM period in these discharges, which have $T_{e,\text{ped}}$ of ~ 150 eV, is compared with that of a high temperature pedestal (up to ~ 300 eV) or low collisionality discharge. The low collisionality discharge, achieved with lower gas fuelling and a modified current ramp up, has a $v_e^* \sim 0.35$, a q_{95} of ~ 5.7 ,

elongation of 1.9, line-averaged density $\langle n_e \rangle = 2.9 \times 10^{19} \text{ m}^{-3}$, a plasma current of 800 kA and B_T on axis of 0.51 T. The 150 eV pedestal discharges have $v_e^* \sim 1.1$, $q_{95} \sim 4.8$, elongation of 1.7, line-averaged density $\langle n_e \rangle = 3.5 \times 10^{19} \text{ m}^{-3}$, a plasma current of 850 kA and a B_T on axis of 0.47 T. Both discharges had similar heating, two neutral beams with a total injected power of 3.4 MW. In the low collisionality discharge the temperature pedestal height as well as the density pedestal height increases between ELMs. A comparison of the pedestal pressure parameter evolution for the two discharges after the ELM are shown in figure 1. During the inter-ELM period for both discharges the position of the edge transport barrier moves inwards and $P_{e,\text{ped}}$ and $\Delta_{pe,\psi}$ increase. The pressure gradient profiles, measured in the final 25% of the inter-ELM period are shown in figure 1(d). The peak $dP_e/d\psi$ obtained in the low collisionality discharge is significantly higher and occurs further inside the plasma. Gyrokinetic analysis of this low collisionality discharge shows that unlike in the high collisionality case [15] the pedestal region is stable to KBMs due to the high bootstrap current which causes low magnetic shear [16].

The EPED [17, 18] model is used to predict the pedestal parameters on a number of different devices [19]. In this model, the pedestal gradient is limited by KBMs, and hence pressure pedestal width scales with pedestal poloidal beta as $\Delta_{pe,\psi} \propto \beta_{\text{poloidal,ped}}^{1/2}$. Pressure pedestal height is separately predicted from peeling–ballooning mode stability and combining these two constraints gives the pedestal operating point. Further to this there has been a number of empirical results showing pedestal width scaling approximately with $\beta_{\text{poloidal}}^x$, where $x \sim 1/2$ [3, 4, 20]. Figure 2 shows the pedestal top and pedestal width evolutions for four different MAST discharges: 400 and 650 kA single null discharges and the two double null discharges discussed earlier in this section. Averaged results of the pedestal parameter evolution at four bins (0–25%, 25–50%, 50–75% and 75–100%) in the inter-ELM period are shown for each discharge. Different symbols represent the different discharges and the size of each symbol represents increasing time within the inter-ELM period. For all discharges except the low v_e^* DND discharge pedestal evolution throughout the inter-ELM period implies an increasing $n_{e,\text{ped}}$ at constant $T_{e,\text{ped}}$. Similarly increasing plasma current from 400 to 600 kA in SND discharges causes an increase in edge pressure through $n_{e,\text{ped}}$. The period 75–100% of the inter-ELM period in the 400 kA discharge has similar pedestal profiles to the period 25–50% in the 600 kA discharge.

For the four discharges shown in figure 2 the HFS pedestal width scaling with β_{poloidal} is examined. All discharges have an injected neutral beam power of ~ 3.4 MW. The discharges have a scaling of pedestal width in the range $\Delta_{pe,\psi} = 0.06\text{--}0.08\sqrt{\beta_{\text{pol}}}$, where the pedestal width is measured in normalized flux space. This scaling is valid both within the inter-ELM period for any given discharge and comparing the pedestal widths at the end of the inter-ELM period for different plasma discharges. The results also show that this scaling holds across magnetic configurations, that is for both single and double null plasmas with their very different geometries.

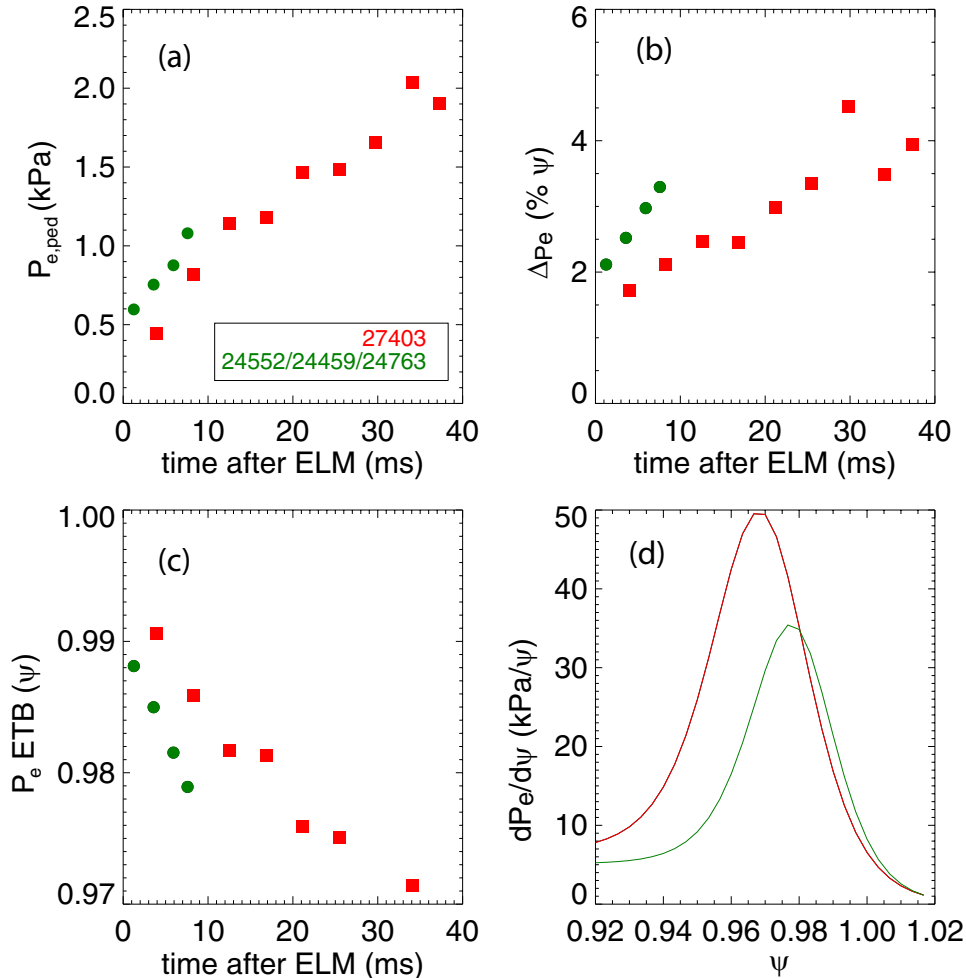


Figure 1. Pressure pedestal evolution between ELMs for a $T_{e,ped} = 150$ eV MAST H-mode discharge (green circles) and for a high temperature pedestal discharge (red squares): (a) pressure pedestal height, (b) pedestal width, (c) edge transport barrier position and (d) pressure gradient profiles for the edge region in the final 25% of the inter-ELM period.

The scaling also holds whether the variation in $\beta_{poloidal}$ is caused by variation in $P_{e,ped}$ at approximately constant I_p as in the high and low ν^* DND plasmas or variation in $P_{e,ped}$ as well as I_p , as in 400 and 600 kA discharges. For this analysis the magnitude of poloidal magnetic field at the plasma circumference is estimated as $B_{pol} = \mu_0 I_p / L_p$ [20] where L_p is the poloidal circumference of the last closed flux surface.

The pressure pedestal widths $\Delta_{pe,\psi}$ and peak gradients $dP_e/d\psi$ on the HFS and LFS behave differently depending on the plasma configuration, as shown in figure 3. As would be expected, for both SND and DND plasmas the pedestal top value, $P_{e,ped}$, observed on the HFS and LFS are identical. In SND plasmas, very similar $\Delta_{pe,\psi}$ and hence similar $dP_e/d\psi$ are observed on the HFS and LFS. By contrast in DND plasmas broader $\Delta_{pe,\psi}$ and lower $dP_e/d\psi$ are observed on the LFS of plasma in flux space. There is typically a flux expansion of ~ 2 from HFS to LFS, which means that in real space there is good agreement in pedestal width LFS to HFS in the DND case and similarly for the pressure gradient as observed in real space. Similar results have been reported previously on MAST [3] obtained using different TS systems (a Ruby TS system and

edge Thomson system) giving a very high degree of confidence in this observation. An implication of different pedestal widths at different poloidal locations in these DND plasmas is that devices where the pressure profile is measured away from the LFS midplane and then mapped using normalized flux may not correspond to actual midplane profiles as is implicitly assumed in the analysis.

3. Application of $n = 6$ RMP field to SND discharges

3.1. Gradient change on application of $n = 6$ RMP field

Figure 4 shows $P_{e,ped}$, peak LFS $dP_e/d\psi$, plasma energy and D_α emission as a function of time for plasma discharges with and without applied RMP field. Similar, but not identical, trends are observed on the HFS as discussed later in this paper. In figure 4 the discharge with the applied RMP field shows a much higher ELM frequency. A decrease in both $P_{e,ped}$ and $dP_e/d\psi$ in the pedestal is observed when the ELM coils are applied. Only points from ELMs in the last 80% of the inter-ELM period are shown, as the gradient observed in the range 0–20% is highly variable. The scatter in the $P_{e,ped}$ and $dP_e/d\psi$

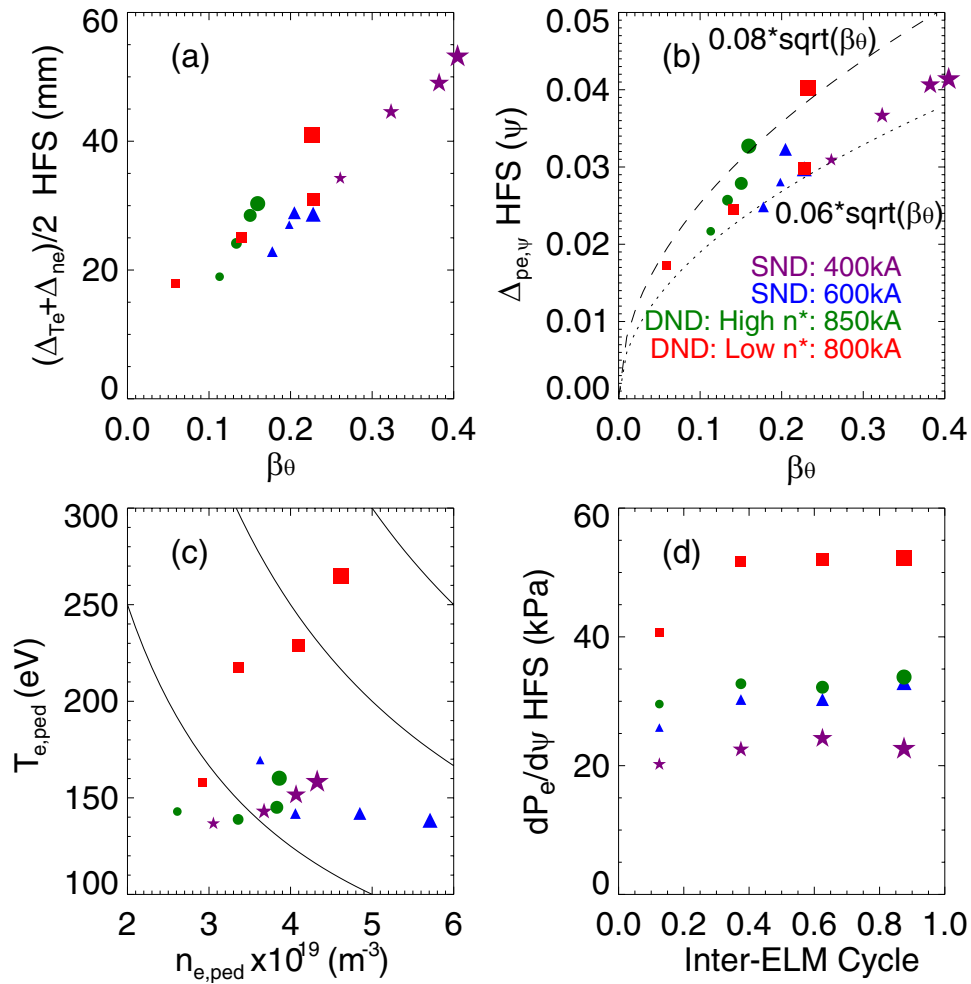


Figure 2. Four MAST discharges shown each represented by a different symbol. Each discharge is evaluated at four times during the inter-ELM period. Increasing time in the inter-ELM period is represented by increasing symbol size: (a) evolution of average of density and temperature pedestal widths in real space, (b) pressure pedestal width in flux versus poloidal beta, (c) pedestal top electron temperature and density and (d) pressure gradient evolution versus time within the inter-ELM period.

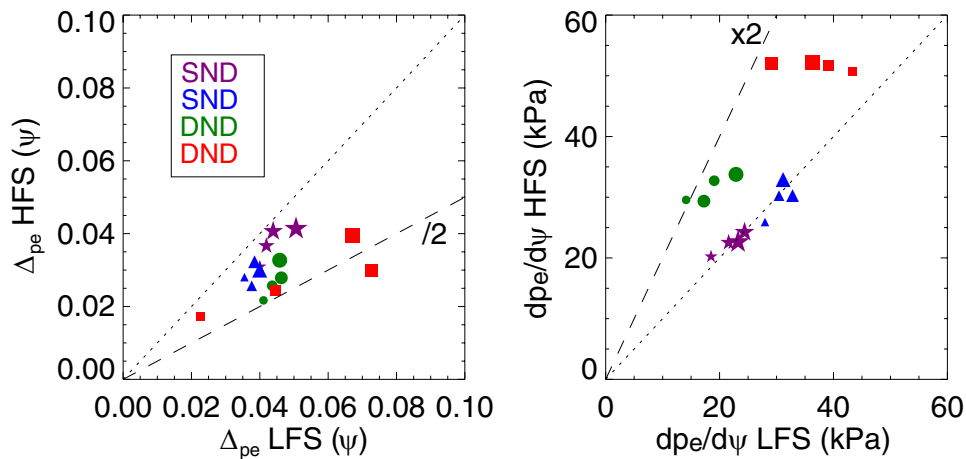


Figure 3. Comparison of the pedestal widths and pressure gradients on the high- and low-field sides of the plasma in single null (SND) and double null (DND) configurations for the same four discharges as in figure 2. Symbol size represents time during the inter-ELM period of the discharge.

shown is due to uncertainty in the measurement and timing of the measurement in the inter-ELM period. During the inter-ELM period $P_{e,ped}$ varies by a factor of two and $dP_e/d\psi$ by $\sim 15\text{--}20\%$. However, the change in $dP_e/d\psi$ upon application

of the RMP is much larger than the measurement scatter. Cases are also observed where the RMP field is applied before the L–H transition, these cases show a lower $dP_e/d\psi$ throughout the discharge than equivalent discharges with no RMP.

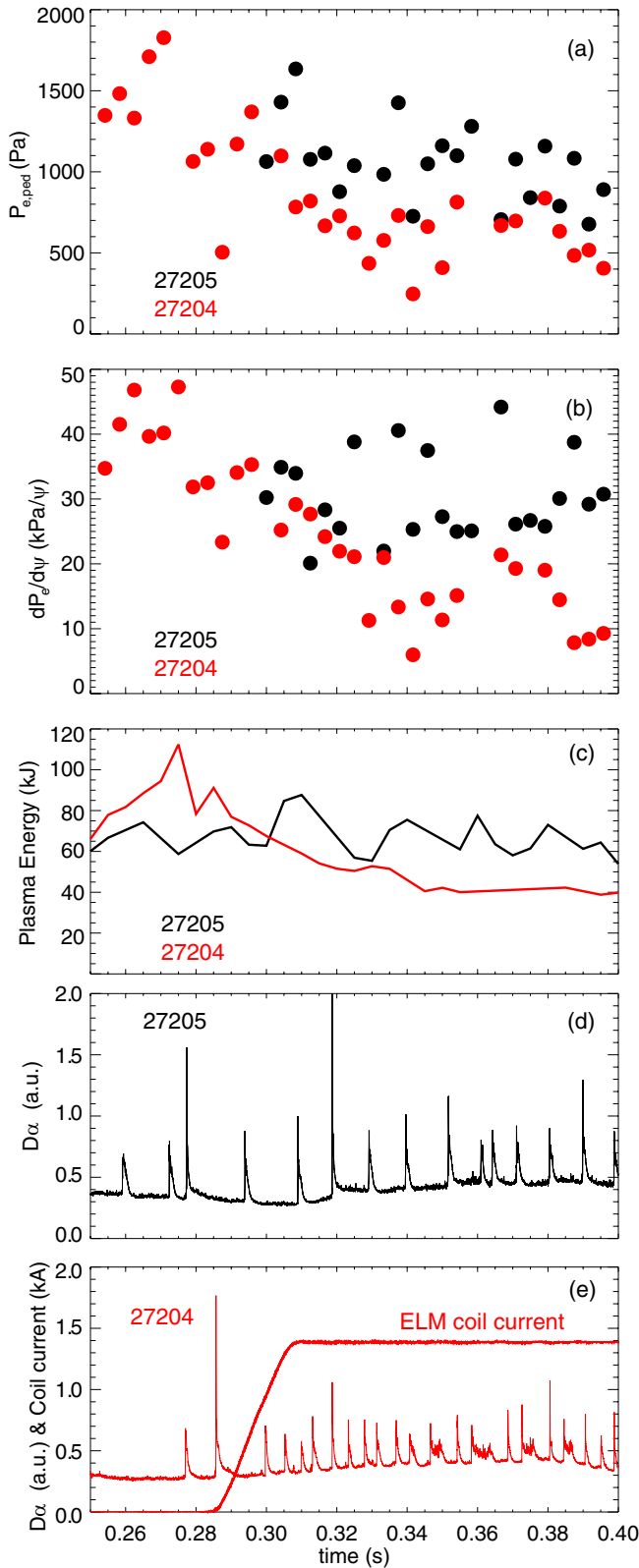


Figure 4. (a) Pressure pedestal height and (b) peak pressure gradient evolution for identical discharges with and without application of 1.4 kA of RMP coil current applied in an $n = 6$ configuration. (c) Total stored plasma energy from magnetic reconstruction. (d) D_α emission for no RMP discharge. (e) D_α emission and coil current for mitigated discharge.

3.2. Radial profiles on application of $n = 6$ RMP field

The radial profiles from two sets of discharges are compared: an ‘RMP on’ dataset with applied $n = 6$ perturbations and an ‘RMP off’ dataset with no applied field. The RMP on dataset contains 69 profiles taken during mitigated H-mode periods of 30–120 ms during three MAST discharges #27204, #27811 and #28002. The RMP off data set contains 75 profiles during three MAST discharges #27205, #27315 and #28158. Other than the current in the RMP coils, these discharges are identical. These discharges had a plasma current of 620 kA, a q_{95} of 2.6 and a pedestal top collisionality of 1.2 and are all in the lower single null (SND) configuration. Both datasets have moderate gas fuelling rates (the implications of different fuelling rates will be discussed later in the paper). The ELM mitigation observed in the RMP on dataset is that there is an increase in ELM frequency from approximately 60 to 200 Hz.

For these RMP on and RMP off datasets the radial profiles in the last 50% of the inter-ELM period are averaged (figure 5). A reduction in $n_{e,ped}$ is observed due to the RMP field caused by increased particle transport, or some other mechanism; however, the two sets of shots have similar T_e profiles. It can be seen that the plasma edge is moved outwards by ~ 30 mm, equivalent to $\sim 6\%$ r/a , on turning on the coils. The observed LFS Δn_e in the ‘RMP on’ shot is increased by 50% with respect to the ‘RMP off’ shot as the plasma edge is moved outwards, an increase in ΔT_e is also observed. In general, decreasing β should cause a decrease in $\Delta\psi$ as per the scaling, hence the increase in Δ (in real space here, but also in flux space as shown later) appears to be a result of RMPs. The HFS of the plasma experiences the density pump out but shows no evidence of change in position or pedestal width due to the application of the RMP field.

The outward movement of the plasma is a toroidally asymmetric perturbation [21] but also includes a plasma control system response due to a drop in β . This system response can be removed by looking at the relative edge radial displacement at two toroidal locations. Figure 6(a) shows the relative radial position of the ETB from mtanh fits to TS data and the D_α peak measurement with and without applied RMPs. The D_α camera images the outboard midplane of the MAST plasma with high resolution, for a full description see [22]. The D_α camera lines of sight go through the vertical midplane, while the TS diagnostic measures 15 mm above the vertical midplane. In these single null discharges, the plasma centre is at $z = -200$ mm and the LCFS of the plasma is steeply angled at the vertical midplane. For this reason the ETB location seen by the TS diagnostic is ~ 10 mm further inside that seen by the D_α camera in the ‘RMP off’ case. The toroidal measurement locations of TS and linear D_α camera are indicated in figure 6(b). The relative radial displacements at the two toroidal locations are compared with the results of the vacuum field line tracing code ERGOS [23] in figure 6(b). These plots show field lines traced for 200 toroidal turns as a function of radial location and toroidal angle. The line colours indicate the minimum normalized flux that the field experiences during its trajectory. In this case the TS measures at close to the maximum edge displacement due to the $n = 6$ RMP and the D_α close to the minimum. Using this ψ as a

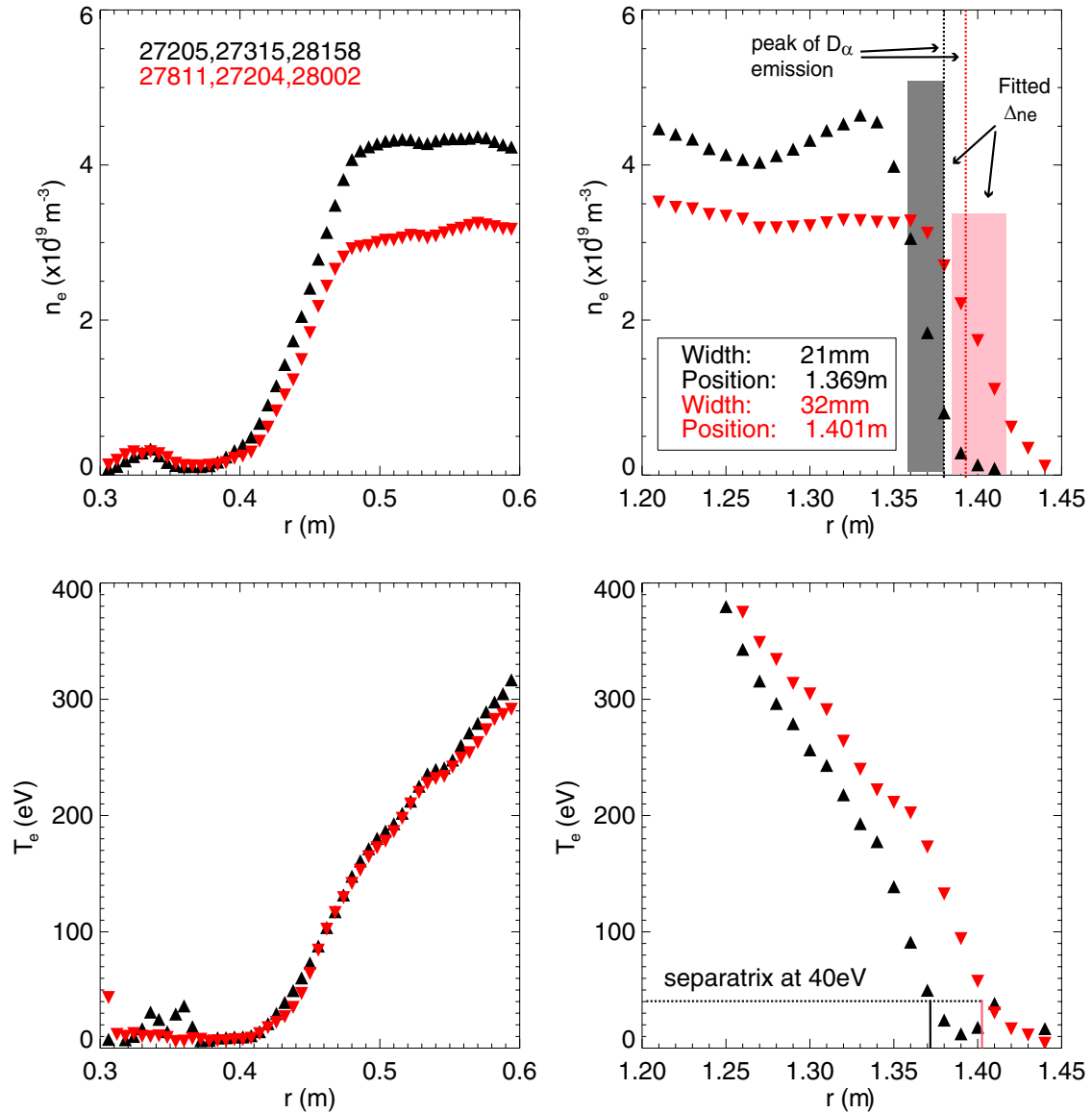


Figure 5. Profiles of edge electron temperature and density for shots without RMP (black) and with applied $n = 6$ RMP fields (red) at the high- and low-field sides of the plasma.

function of radius and toroidal angle from ERGOS the radial displacement of the ETB at the toroidal locations of the D_α and TS diagnostics is calculated to be ~ 18 mm, which agrees well with the direct measurements in figure 6(a).

3.3. Pedestal profile evolution during application of $n = 6$ RMP fields

Figure 7 shows the pedestal parameter evolution for the RMP on and RMP off datasets for data collected from the LFS of the plasma. The RMP on and off datasets are binned as a function of time through the inter-ELM period. Comparing the pedestal top values at the same time after the ELM, the $T_{e,\text{ped}}$ is similar while $n_{e,\text{ped}}$ and $P_{e,\text{ped}}$ show a reduction of approximately 10% with the RMP on. The density and temperature pedestal widths as measured in real space at the same time after an ELM are observed to be significantly larger in the RMP on case, with the exception of the first bin after

the ELM collapse. However, for up to 1 ms after the ELM it is difficult to accurately measure pedestal parameters, so this bin is not particularly useful for comparison purposes. As well as expansion of Δ_{n_e} and Δ_{T_e} in real space due to applied RMP, using EFIT mapping to normalized flux without the knowledge of a toroidal perturbation, a similar expansion of $\Delta_{pe,\psi}$ is observed. A phenomenon such as island structures, reported to exist in the pedestal during RMP experiments on DIII-D [5], could lead to increased pedestal widths being observed.

A comparison of $dP_e/d\psi$ on the HFS and LFS of the plasma before and after application of the RMP field is shown in figure 8. With no applied field, similar pedestal widths and gradients are observed HFS and LFS, as is typical for all SND discharges on MAST. Upon application of the applied field there is a collapse in pressure gradient of 30–50% due to $n_{e,\text{ped}}$ decrease on both HFS and LFS of the plasma. This collapse in gradient is larger on the LFS due to an increase in pedestal width, whilst no increase in pedestal width is observed on the HFS.

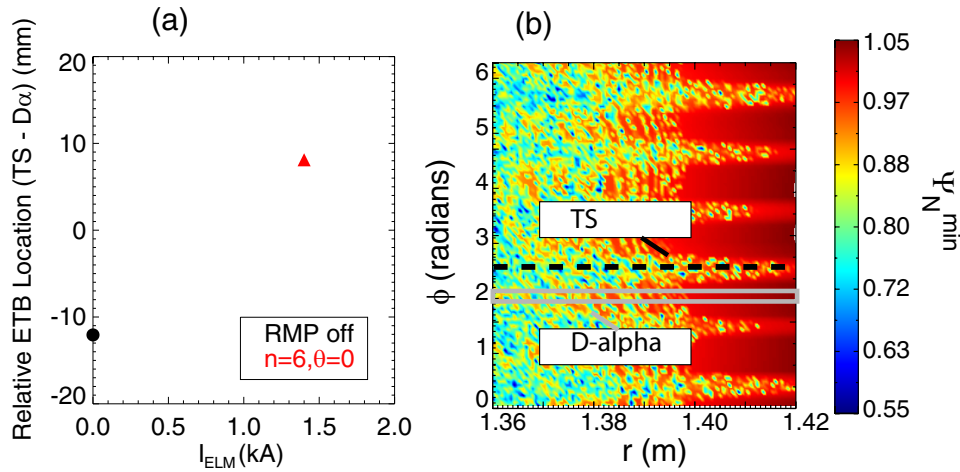


Figure 6. (a) Edge transport barrier position obtained from Thomson scattering profiles relative to the peak of D_α signal. (b) ERGOS simulation of plasma with applied $n = 6$ perturbations showing toroidal measurement locations of TS and D_α measurements.

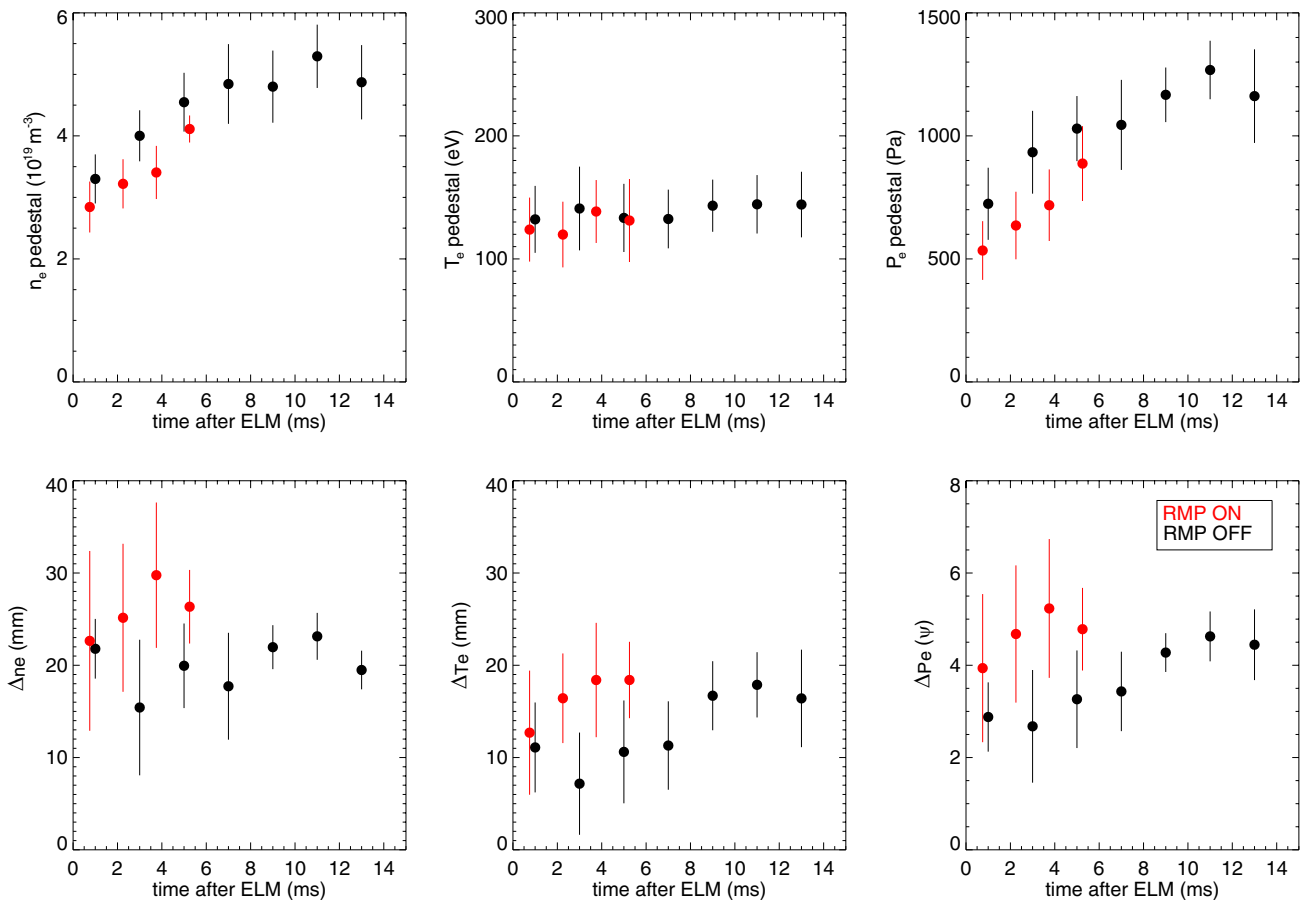


Figure 7. Evolution in the inter-ELM of pedestal parameters on low-field side with RMP off and an RMP coil current of 1.4 kA in an $n = 6$ applied perturbation.

4. Variation of pressure gradient with fuelling and RMP

Discharges with different gas fuelling levels and RMP coil currents, with applied fields of both $n = 4$ and $n = 6$ are examined and the results are summarized in figure 9. All discharges have the same injected neutral beam power of 3.4 MW. With no additional gas fuelling coil currents of 1 kA cause approximately a doubling in ELM frequency and

currents of 1.4 kA typically result in a back transition to L-mode. In shots with refuelling, currents of 1.4 kA cause a similar increase in ELM frequency and no back transition, for more details see [24]. Hence in figure 9, a discharge without refuelling and 1 kA of coil current is compared with discharges with refuelling and 1.4 kA of coil current.

The n_e - T_e diagram in figure 9 shows that for a plasma no refuelling during the applied RMP, 1 kA of RMP current causes a reduction in $n_{e,ped}$ and a significant increase in $T_{e,ped}$. The

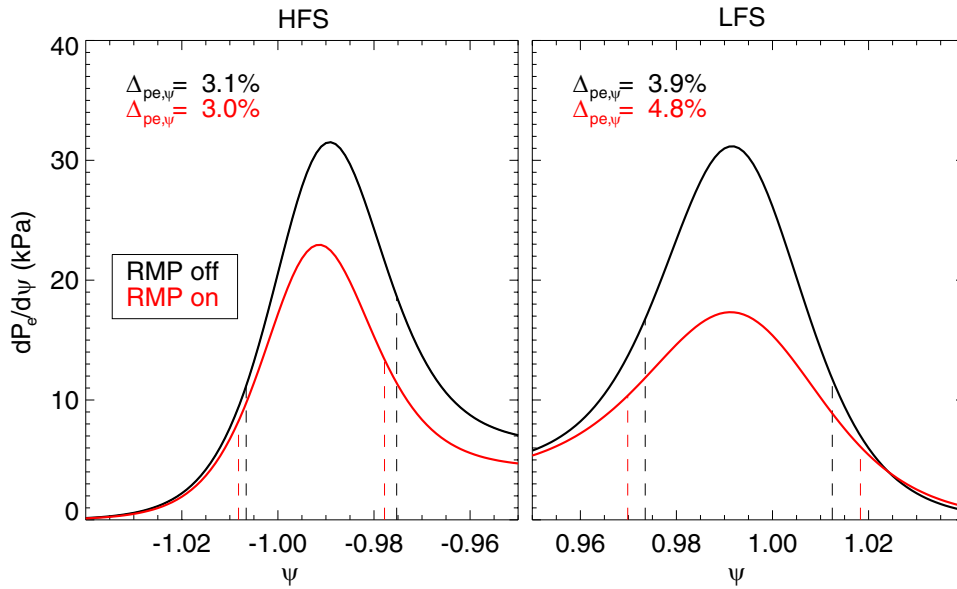


Figure 8. Comparison of pressure gradients within the pedestal with and without RMP coils as measured at the high- and low-field sides of the plasma. Vertical dashed lines indicate the measured pedestal widths.

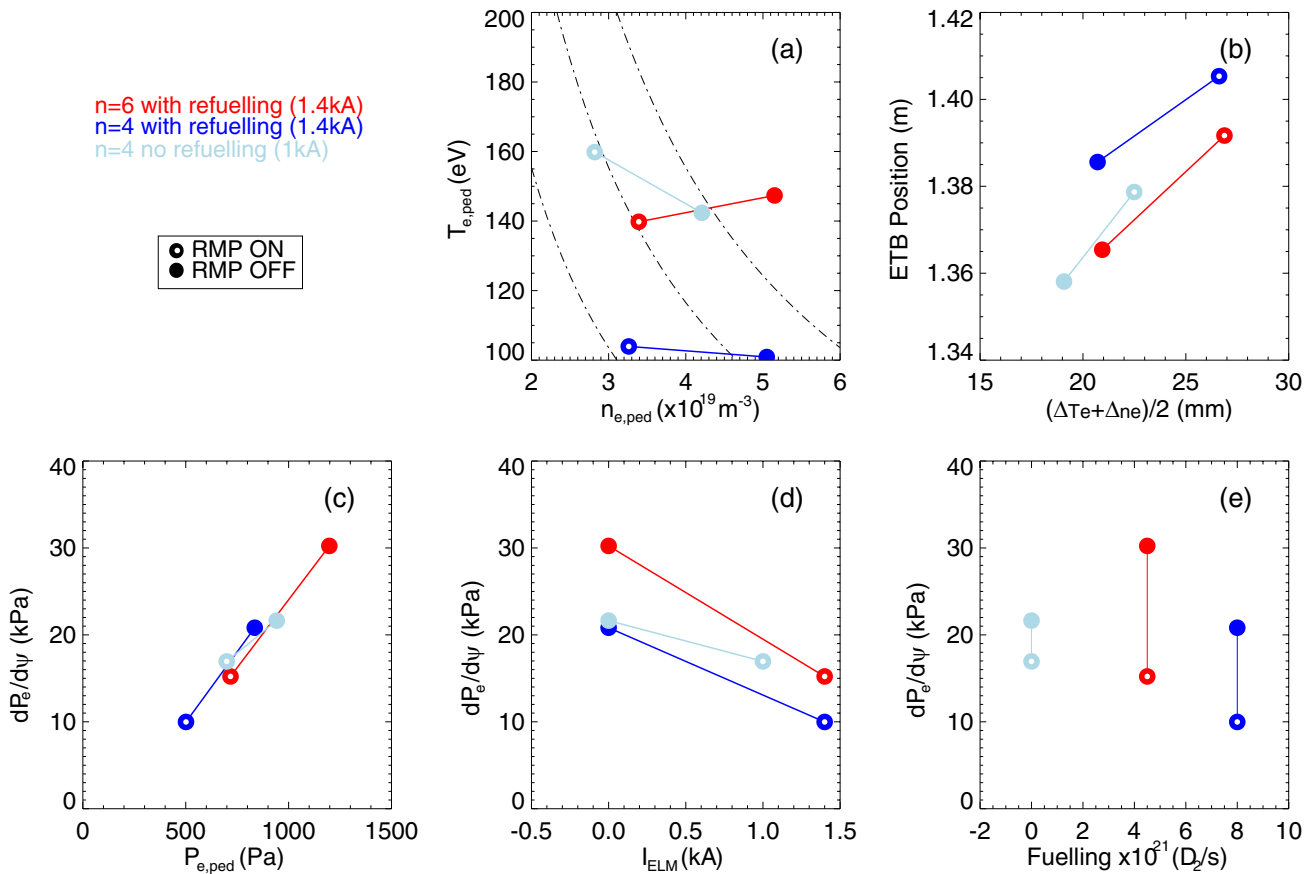


Figure 9. Impact of turning on ELM coils for three different MAST discharges. In all cases the filled symbol represents the RMP off discharge and the hollow symbol the RMP on discharge. (a) Temperature and density pedestal, (b) edge position and pedestal width change, (c) pressure gradient and pressure pedestal height, (d) pressure gradient change with coil current and (e) pressure gradient change with gas fuelling.

increase in $T_{e,ped}$ is likely due to increased heating power per particle in the lower density plasma. In the refuelling cases with 1.4 kA in the RMP coils there are larger decreases in $n_{e,ped}$ and little or no increase in $T_{e,ped}$. The lack of increase in

$T_{e,ped}$ may be due to the increase in heating power per particle being outweighed by the increased recycling due to higher neutral pressure. A moderate amount of gas fuelling, as seen in figure 9(e), is optimal for typical MAST discharges and allows

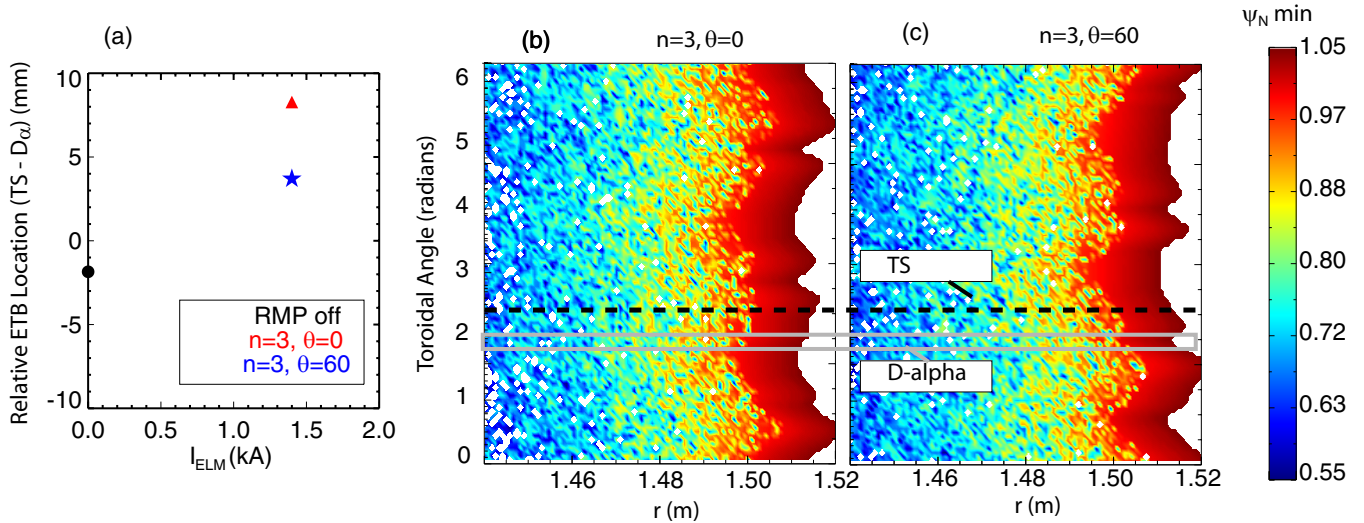


Figure 10. (a) change in position of edge transport barrier as measured by Thomson scattering for application of $n = 3$ error fields with a phase of 0° and 60° . (b) ERGOS simulation for case of $n = 3, 0^\circ$ (c) ERGOS simulation for the case of $n = 3, 60^\circ$.

them to reach higher $P_{e,ped}$ and $dP_e/d\psi$ than discharges with no fuelling or very high fuelling. Application of RMP field due to 1.4 kA of coil current to these moderately fuelled shots reduces $P_{e,ped}$ and $dP_e/d\psi$ to the same level as 1.0 kA of coil current in the unfuelled discharges.

An outward displacement of the plasma edge and increase in pedestal width are observed on the LFS of the plasma in all discharges examined in figure 9(b). Edge displacement and pedestal width expansion both increase with increasing RMP coil current, although the effects of fuelling cannot be separated out.

5. Application of $n = 3$ fields to double null discharges

The toroidal variation of edge displacement can be examined by applying different phases of the same perturbation and measuring at a fixed toroidal location. In this section, edge profiles during application of $n = 3$ error fields with phases of 0° and 60° are compared. Ideally measurements at the minimum and maximum of the radial perturbation due to the RMP would be obtained; however, TS measurements in this case are somewhere between.

For discussion of DND plasmas ELM coil parity must be mentioned. There are two rows of ELM coils one above and one below the midplane. Even parity means that coils in the same toroidal location in upper and lower rows have the same current, odd parity means that these coils have the opposite current. For the DND plasmas discussed here the coils are in even parity. For SND plasmas discussed previously only the lower row of coils are active, hence parity is not an issue.

Figure 10(a) shows the relative radial position of the ETB from mtanh fits to TS data and the D_α peak measurement for different applied RMPs. For DND plasmas the centroid of the plasma is at $z \sim 0$ mm. Hence the 15 mm vertical separation between the D_α and TS lines of sight has little impact on the observed radial position of the LCFS by the two diagnostics.

For no applied field the ETB position from the two diagnostics agrees well. Application of an $n = 3, 0^\circ$ perturbation causes a toroidally local outward movement of the TS ETB with respect to the D_α ETB of ~ 10 mm for an $n = 3, 0^\circ$ RMP field. An outward movement of ~ 6 mm is observed for a $n = 3, 60^\circ$ field.

The relative radial displacements at the two toroidal locations can be compared with the predictions of the vacuum field line tracing code ERGOS in figures 10(b) and (c). The predicted magnitude of the edge perturbation in this case is ~ 10 mm which is much smaller than the SND case (figure 6) where perturbations of 30 mm are predicted by ERGOS. The smaller offset in position between D_α and TS which is observed, agrees with the ERGOS prediction. The relative change in TS and D_α ETB in going from $n = 3, 0^\circ$ to 60° applied RMPs also agrees with the ERGOS prediction. However, the offset between the TS and D_α ETB for the coils on cases relative to the coils off cases is larger than that predicted by ERGOS. A further experiment is planned where the $n = 3$ perturbation will be rotated in the view of the TS and D_α diagnostics, which will provide more detailed toroidal sampling of the RMP edge perturbation.

The LFS pedestal evolution in the inter-ELM for this DND case, shown in figures 11(a) and (b), is similar to SND discharges with ELM coils: $n_{e,ped}$ increases in line with the ‘RMP off’ $n_{e,ped}$ except that the increase is terminated by an ELM sooner and larger pedestal widths are observed with RMP on. The observed Δn_e for $n = 3, 0^\circ$ RMP is marginally larger than those for the 60° phase shifted RMP. Although the width difference between the two phases of perturbation is within the measurement uncertainty, Δn_e are clearly larger with RMP on than off.

Figure 11(c) shows the stability analysis using ELITE [25, 26] for an RMP off case and a $n = 3, 0^\circ$ applied field case for individual profiles taken in a 1 ms time window before an ELM is triggered. Without applied RMP perturbations, the plasma is very close to the stability limit just before the ELM. With applied RMP perturbation the plasma is far from the

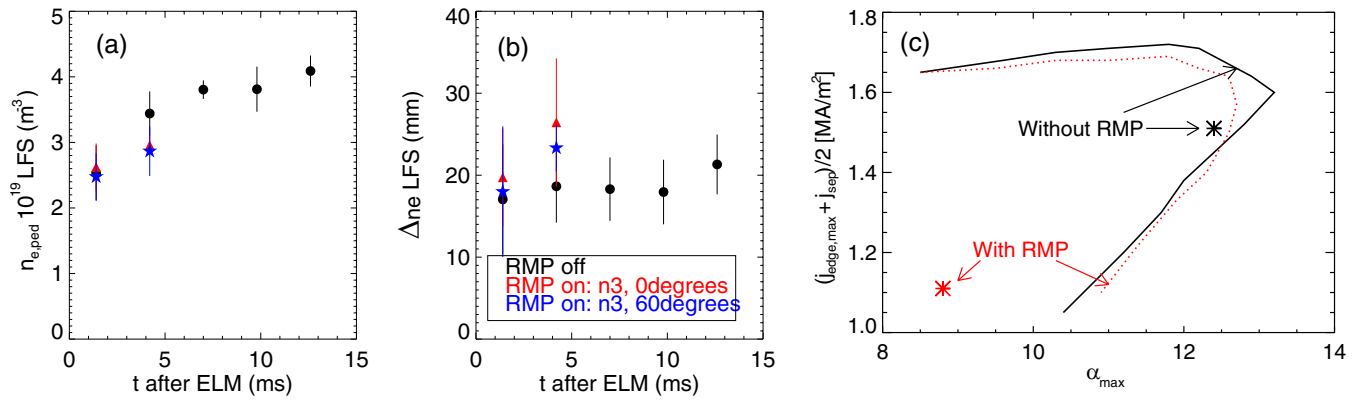


Figure 11. (a), (b) Pedestal density and width evolution in the inter ELM for different phases of error fields. (c) Edge stability to both ‘RMP off’ and ‘RMP on: $n = 3, 0^\circ$ ’ profiles taken at the end of the inter-ELM period to $n = 5, 10, 15, 20, 25$ modes. Since there is an overlap of pedestal widths in the coils on and off datasets, the stability analysis shown here is for cases with similar widths.

stability limit, hence the subsequent triggering of an ELM must be explained by other means. ELMs triggered in this stable region during application of RMP have also been observed in SND plasmas [27], where it is proposed that perturbations near the x-point are the mechanism for degrading the peeling–ballooning stability boundary.

6. Summary

The first part of this paper examines discharges without RMP. In these discharges, the pressure gradient in the pedestal does not change significantly during the final 75% of the inter-ELM period. For a given discharge, this approximately constant $dP_e/d\psi$ during the inter-ELM period occurs because $\Delta_{pe,\psi}$ increases with β_θ to compensate for $P_{e,ped}$ increase between ELMs. The same pedestal width scaling observed during the inter-ELM period of a given discharge is also observed between discharges at different I_p and for different magnetic configurations. In single null plasmas the same $\Delta_{pe,\psi}$ and $dP_e/d\psi$ are observed at the HFS and LFS of the plasma. However, in double null plasmas $\Delta_{pe,\psi}$ is larger and hence $dP_e/d\psi$ is lower on LFS of the plasma. This has implications for other machines where measurements of the transport barrier are mapped to the LFS mid-plane.

Applying an RMP field to the plasma causes a particle ‘pump out’ resulting in a significant decrease in pressure gradients. On the LFS of the plasma the RMP also causes toroidally local outward displacements of the plasma edge and toroidally local increases in pedestal width. The pedestal width on the HFS of the plasma is unaffected by the perturbation which is observed only at the LFS. This results in poloidally asymmetric pressure gradients in SND discharges during RMPs. In the case of an $n = 6$ RMP applied to an SND plasma a reduction in $dP_e/d\psi$ on the HFS of $\sim 30\%$ (decrease in $P_{e,ped}$, constant $\Delta_{pe,\psi}$) is observed as against $\sim 50\%$ on the LFS (decrease in $P_{e,ped}$, increase $\Delta_{pe,\psi}$). This strongly reduced pressure gradient would imply greater stability to MHD, but is observed to exist with increasing ELM frequency. Pedestal evolutions in the inter-ELM period are similar with and without the applied perturbation with the difference that, when there

is an applied perturbation, the evolution is terminated by an ELM much sooner.

A second case examined was the application of $n = 3$ field at toroidal angles of 0° and 60° to a DND plasma. Much smaller LCFS perturbations are predicted by ERGOS for this case, ~ 10 mm as opposed to ~ 30 mm for the $n = 6$ case. A smaller radial perturbation was observed between the TS and D_α diagnostics in line with the prediction. An expansion in pedestal width was also observed. Since the TS system does not measure at the toroidal minimum of the RMP field it is not yet known if $\Delta_{pe,\psi}$ does not expand at this point and hence if there is a toroidally local higher $dP_e/d\psi$ at these RMP minima. Further experiments investigating the toroidal variation of the pressure profile during RMP are planned.

Acknowledgments

This work was funded by the RCUK Energy Programme under the grant EP/I501045 and the European Communities under the contract of Association between Euratom and CCFE. The views expressed herein do not necessarily reflect those of the European Commission.

References

- [1] Schneider P A *et al* 2012 *Plasma Phys. Control. Fusion* **54** 105009
- [2] Beurskens M *et al* 2011 *Phys. Plasmas* **18** 056120
- [3] Kirk A *et al* 2009 *Plasma Phys. Control. Fusion* **51** 065016
- [4] Urano H *et al* 2008 *Nucl. Fusion* **48** 045008
- [5] Evans T *et al* 2008 *Nucl. Fusion* **48** 024002
- [6] Kirk A *et al* 2011 *Plasma Phys. Control. Fusion* **53** 065011
- [7] Suttrop W *et al* 2011 *Plasma Phys. Control. Fusion* **53** 124014
- [8] Fischer R *et al* 2012 *Plasma Phys. Control. Fusion* **54** 115008
- [9] Mordijck S *et al* 2012 *Phys. Plasmas* **19** 056503
- [10] Dickinson D *et al* 2011 *Plasma Phys. Control. Fusion* **53** 115010
- [11] Liang Y *et al* 2007 *Phys. Rev. Lett.* **98** 265004
- [12] Scannell R *et al* 2010 *Rev. Sci. Instrum.* **81** 10D520
- [13] Scannell R *et al* 2011 *Rev. Sci. Instrum.* **82** 053501
- [14] Groebener R J and Carlstrom T N 1998 *Plasma Phys. Control. Fusion* **40** 673
- [15] Dickinson D *et al* 2012 *Phys. Rev. Lett.* **108** 135002

- [16] Saarelma S *et al* 2012 *EPS Conf. (Stockholm, Sweden)*
[17] Snyder P B *et al* 2011 *Nucl. Fusion* **51** 103016
[18] Snyder P B *et al* 2009 *Phys. Plasmas* **16** 056118
[19] Beurskens M *et al* 2009 *Plasma Phys. Control. Fusion* **51** 124051
[20] Diallo A *et al* 2011 *Nucl. Fusion* **51** 103031
[21] Chapman I T *et al* 2012 *Plasma Phys. Control. Fusion* **54** 105013
[22] Tournianski M *et al* 2003 *Rev. Sci. Instrum.* **74** 2090
[23] Nardon E *et al* 2007 *J. Nucl. Mater.* **363** 1071
[24] Kirk A *et al* 2013 *Plasma Phys. Control. Fusion* **55** 015006
[25] Wilson H R, Snyder P B, Huysmans G T A and Miller R L 2002 *Phys. Plasmas* **9** 1277
[26] Snyder P B *et al* 2002 *Phys. Plasmas* **9** 2037
[27] Chapman I T *et al* 2012 *Nucl. Fusion* **52** 123006